Author Manuscript
Author Manuscript
Author Manuscript
Author Manuscript

HHS Public Access
Author manuscript
Bioconjug Chem. Author manuscript; available in PMC 2019 November 21.

Published in final edited form as:
Bioconjug Chem. 2018 November 21; 29(11): 3691–3704. doi:10.1021/acs.bioconjchem.8b00611.

Histone-Mimetic Gold Nanoparticles as Versatile Scaffolds for Gene Transfer and Chromatin Analysis

Erik V. Munsell[†], **Bing Fang**[†], and **Millicent O. Sullivan**[*]
Department of Chemical and Biomolecular Engineering, University of Delaware, 150 Academy Street, Newark, DE 19716 United States of America

Abstract

Histone-inspired polymer assemblies (polyplexes) can regulate gene expression and subcellular transport in plasmids by harnessing the cellular machinery normally used for histone proteins. When grafted to polyplexes, histone tails promote nuclear accumulation, trigger plasmid DNA (pDNA) release, and enhance transcription. Herein, we developed multifunctional gold nanoparticles (AuNPs) decorated by histone motifs as histone-inspired scaffolds with improved pDNA binding, easy bioimaging, and increased potential for gene delivery and chromatin analysis applications. We hypothesized that polycationic AuNPs coupled to histone motifs would mimic the native presentation of these sequences on the histone octamer and thereby create structures with the capacity to both engage native histone effectors and condense pDNA into nucleosome-inspired nanostructures. AuNPs bearing ~2 nm cores were prepared based on the well-established Brust-Schiffrin two-phase method involving tetrachloroaurate reduction in the presence of 1-pentanethiol. Solid phase peptide synthesis was employed to generate thiolated polycationic ligands and histone tail motifs, and the AuNPs and peptide ligands were combined in a 2-step Murray place exchange reaction at various ratios to produce a collection of polycationic AuNPs modified with varying amounts of histone tails. Electron microscopy and thermal analyses demonstrated that these modified AuNPs exhibited tunable biochemical and biophysical properties that closely mimicked the properties of native histones. The histone-mimetic nanoscaffolds efficiently and sequence-specifically engaged histone effectors responsible for activating transcription. In addition, the nanoscaffolds condensed pDNA into complexes with high stability in the presence of physiological concentrations of heparin, a common extracellular polyanion. These combined properties of histone engagement and high stability led to a ~6-fold enhancement in transfection efficiency as compared with typical polymeric transfection reagents, with the increased transfection efficiency correlated to the presence and amount of histone tails displayed on the surface of the nanoscaffolds. These findings demonstrate the utility of employing a

[*]Correspondence should be addressed to M.O.S. Department of Chemical & Biomolecular Engineering, University of Delaware, 150 Academy St., Newark, DE 19716, msullivan@udel.edu, +1-302-831-8072 (p), +1-302-831-1048 (f).
[†]These authors contributed equally to this work

Conflicts of Interest
The authors declare no competing conflicts of interest.

Supporting Information
Synthetic schemes and molecular characterizations (NMR and MS) of MUA, H3-MUA, and K5-MUA; CHNS elemental analysis results; pull-downs with anti-FLAG antibodies; TEM images of K5AuNP-pDNA complexes; cellular viability analyses; and transfection efficiencies of low- and mid-H3 AuNP/PEI hybrid complexes

Author Manuscript Author Manuscript Author Manuscript Author Manuscript

biomimetic materials design approach to develop more effective and stable delivery vehicles for gene transfer and chromatin analysis applications.

Graphical Abstract

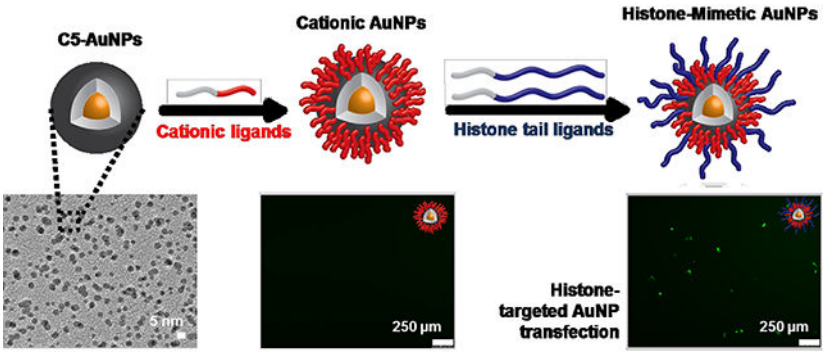

Introduction

Nanoparticles have shown enormous promise in applications ranging from catalysis to biology, leading to an explosion of nanotechnology development in the past decade.[1–4] Nanoparticle methods offer improved imaging potential, versatile chemistries, and high surface area to volume ratios that enable efficient surface modification for drug delivery and other applications.[5, 6] For example, gold nanoparticles (AuNPs) possessing 2 nm core diameters can accommodate ~100 surface ligands incorporating targeting moieties and/or therapeutic materials.[7, 8] Moreover, AuNPs can initiate cellular entry with unprecedented efficiency.[9–11] Additionally, AuNPs have a promising safety profile based on clinical analyses of bulk gold and recent evaluations of gold nanostructures,[12] with nanogold spheres (d > 1–2 nm) showing minimal toxicity both in cell culture[13–15] and following either local or systemic administration.[16]

Given their beneficial properties, AuNPs with controlled dimensions and a range of surface modifications have been intensely studied for biosensor applications,[17–20] drug delivery,[21–23] and bioimaging.[24–26] AuNPs offer especially exciting potential in gene transfer applications, with their chemical versatility and high surface area enabling creation of polycationic AuNPs with strong nucleic acid association.[27–32] Additionally, nanogold has been widely used to image gold nanocarriers during *in vivo* and/or intracellular transport, lending new insights into nanocarrier delivery mechanisms.[33–38] Furthermore, the facile surface modification of AuNPs with peptides and other ligands has proven useful for altering the cellular/intracellular transport and fate of AuNPs, enabling improved cytosolic delivery of siRNA[39–41] and proteins,[42, 43] and enhancing AuNP localization in specific cells (e.g., cancer cells).[44–47] Meanwhile, changes in ligand surface density have been shown to alter AuNP intracellular distributions.[48]

Building off of these fundamental insights, we hypothesized that combining H3 tail motifs with polycationic AuNPs would function to mimic the native H3 presentation on the nucleosome, creating nanostructures with the capacity to stably bind as well as controllably

Author Manuscript Author Manuscript Author Manuscript Author Manuscript

deliver plasmid DNA (pDNA). We posited that this biomimetic presentation of the H3 tail motif would better recapitulate native interactions with histone effectors (Figure 1), thus directing nuclear delivery efficiency and transcriptional activation. In addition, the well-established methods for AuNP surface functionalization would facilitate manipulation of peptide displays, enabling tunable pDNA association and controlled recruitment of nuclear effectors involved in transcription. Thus, extracellular stability and intracellular transcription could be simultaneously optimized.

AuNPs with low dispersity and small (~2 nm) core dimensions can be readily prepared by the well-established Brust-Schiffrin method involving hydrogen tetrachloroaurate ($HAuCl_4$) reduction with sodium borohydride ($NaBH_4$) in the presence of 1-pentanethiol (C5-SH).[49] These monolayer-protected AuNPs provide an ideal scaffold for post-functionalization via Murray place-exchange with various combinations of organic ligands,[50] providing a straightforward route to create histone-inspired AuNPs. Herein, we created monolayer-protected AuNPs functionalized with a tunable mixture of polylysine peptides and histone H3 tail peptides whose size and surface chemistries mimicked those of the core histones in the native nucleosome (Figure 1). Our data show that H3 tail peptide densities could be varied on monolayer-protected AuNPs over a range of 4–67 ligands, enabling similar or higher peptide densities than those found in the histone octamer. Subsequently, we evaluated whether these histone-mimetic nanoscaffolds would promote efficient histone effector engagement and permit AuNP-pDNA assembly into nucleosome-like structures that could efficiently deliver pDNA. We showed that the histone-mimetic nanoscaffolds demonstrated a 3-fold higher association with the H3-specific transcriptional activator HBO1 as compared to AuNPs with similar zeta potentials but no H3 tail peptide modifications. Furthermore, the histone-inspired nanoscaffolds formed highly stable complexes with pDNA that displayed substantially better stability against heparin displacement than standard polymeric transfection reagents made with polyethylenimine (PEI). In fact, the AuNP-pDNA complexes were able to preserve transfection efficiency in the presence of heparin concentrations similar to those found in the extracellular environment, whereas PEI polyplexes exhibited a 9-fold decrease in transfection efficiency in the presence of heparin. Gene delivery was clearly driven by the H3 tail peptides, with ~6-fold enhanced transfection efficiencies in H3-modified AuNPs as compared with unmodified-AuNPs. These novel findings represent a significant design advance in gene delivery materials that addresses crucial barriers in pDNA binding stability and nuclear targeting.

Results and Discussion

Preparation of Histone-Mimetic Nanoscaffolds

The histone-mimetic nanoscaffolds were composed of a gold core coated with a layer of thiolated peptide ligands (Figure 2). Peptides were covalently modified with a triphenylmethyl-protected mercaptoundecanoic acid (MUA) alkanethiol chain to help drive the place-exchange reaction and confer stability of the final nanoscaffolds. The initial Brust-Schiffrin synthesized AuNPs were covered and stabilized by a monolayer of C5-SH chains. To endow the AuNP surface with the appropriate charge and functionalization for aqueous solubility and pDNA binding capacity, different combinations of peptide ligands were

Author Manuscript Author Manuscript Author Manuscript Author Manuscript

installed onto the AuNP surface by a 2-step Murray place exchange process.[50] First, ligands containing a short cationic sequence comprised of 5 lysine residues (K5-MUA) were exchanged onto the surface of the C5 AuNPs (Figure 2). The resulting cationic and water-soluble K5 AuNPs were then used in a second place exchange reaction with ligands containing residues 1–25 of the H3 tail (H3-MUA). The final amount of H3 tail displayed on the surface of the resulting histone-mimetic nanoscaffolds was tuned by varying the amount of H3 tail ligand present during the second place exchange. Using this 2-step place exchange procedure, we generated a collection of cationic AuNPs ranging from AuNPs with no H3 ligands to AuNPs that were completely covered with the H3 tail.

AuNP Surface Ligand Composition

In order to determine the degree of AuNP ligand functionalization, thermogravimetric analysis (TGA) and carbon-hydrogen-nitrogen-sulfur (CHNS) elemental analysis were employed. The number of C5 ligands on the precursor AuNP surface was calculated using only TGA analysis due to the simple composition of the monolayer. TGA showed that the C5 AuNP precursors contained ~96 C5-SH surface ligands based on a weight loss of 16.89% from TGA (Figure 3A), which is in good agreement with ligand density estimations in previous studies employing Brust-Schiffrin syntheses.[50–52]

The number of K5-MUA ligands present on the AuNP surface following the first place exchange reaction was analyzed by combining results from TGA (Figure 3B) and CHNS elemental analysis (Table S1). TGA established a weight loss of 38.92% for the K5 AuNPs, which is substantially higher than the weight loss from the C5 AuNP precursors. CHNS elemental analysis enabled calculation of a peptide composition of 31 K5-MUA ligands per K5 AuNP, which is somewhat low as compared to the total number of initial C5-SH ligands present on the precursor AuNP surface. This relatively low density may be a result of the dramatic difference in solubility between the C5-SH and K5-MUA ligands. Specifically, the first place exchange reaction was conducted in a mixture of dichloromethane (DCM) and methanol (MeOH) in order to maintain adequate solubility of both the precursor AuNPs and the K5-MUA peptide ligands. A 2-fold molar excess of K5-MUA ligands to C5 surface ligands was utilized to ensure a high degree ligand exchange, based on previous studies of exchange dynamics.[50] However, due to the significant solubility difference between the C5-SH and K5-MUA ligands, it is likely that the AuNPs containing multiple K5 peptides precipitated out of the mixed solvent before complete exchange could take place. The K5 AuNP product was only soluble under aqueous conditions. TGA and CHNS analyses indicated that the residual C5-SH ligands only occupied ~13 wt% of the K5 AuNP surface, consistent with their high solubility in aqueous media.

The second place exchange reaction was designed such that the H3-MUA ligands would replace a fraction of both the K5-MUA ligands and the residual C5-SH ligands on the AuNP surface. Since the K5 AuNPs and the H3-MUA peptide ligands both readily dissolved in water, the number of H3 ligands on the AuNP surface could be reasonably controlled by tuning the feed ratio of H3-MUA ligands to surface ligands. Three different ratios of H3-MUA ligands to AuNP surface ligands were tested in the place exchange reaction: a ‘low-coverage’ ratio of 0.6:1 (H3:K5); a ‘mid-coverage’ ratio of 1:1; and a ‘high-coverage’ ratio

Author Manuscript Author Manuscript Author Manuscript Author Manuscript

of 2:1. Following the removal of any remaining free ligands, the final histone-mimetic nanoscaffolds were subjected to TGA (Figures 3C, 3D, and 3E) and CHNS analysis (Table S1). TGA yielded 54.1%, 57.1%, and 81.1% weight losses for the low-, mid-, and high-H3 AuNPs, respectively. These results were combined with CHNS analysis to estimate the surface ligand compositions in the three different H3-containing mixed monolayer AuNPs, as reported in Table 1.

AuNP Core and Surface Property Characterization

In order to determine whether the modified AuNPs were of the small size required to mimic native nucleosome dimensions, both the core diameter and the core dispersity were analyzed by transmission electron microscopy (TEM) as shown in Figure 4. Quantitative image analysis (Figure 4B) illustrated that the mean core diameter was ~2.5 nm, with a relatively narrow distribution of diameters ranging from 1.5 nm to 3.5 nm. Magnified images (Figures 4C and 4D) show the lattice-like structure of the gold core with a lattice spacing of ~2.4 Å, and the characteristic crystallographic planes of face-centered cubic gold.[53] The contrast in TEM did not provide noticeable detail of the structures in the surrounding ligand layer.

Although TEM demonstrated that the AuNPs possessed a small core, the TEM measurements did not allow assessment of the size and surface properties of the AuNP after functionalization with the peptide layer. Accordingly, dynamic light scattering (DLS) and zeta potential analyses were used to assess the peptide-functionalized AuNPs in aqueous solution. DLS demonstrated a significant increase in hydrodynamic diameter in both the K5 AuNPs and the histone-mimetic AuNPs as compared with the C5-modified gold core. The average hydrodynamic diameter of the K5 AuNPs was 22 nm (Table 1). This diameter increased ~5-fold following installation of the longer H3-MUA peptide ligand. Average hydrodynamic diameters of low-, mid-, and high-H3 AuNPs increased with increasing H3 ligand densities (59 nm, 74 nm, and 99 nm, respectively). Meanwhile, the zeta potentials of the modified AuNPs ranged from 25 to 50 mV in 4-(2-hydroxyethyl)-1-piperazineethanesulfonic acid) (HEPES) buffer (Table 1). A slight decrease in zeta potential was observed after the low H3-MUA ligand addition onto the AuNP surface, and there was a subsequent increase in zeta potential as more H3-MUA ligands were attached.

The installation of cationic ligands onto the AuNP surface resulted in positive zeta potential measurements as expected, and indicated a positively charged shear plane of the particles. However, the observed differences in zeta potential between different species of surface-modified AuNPs were not initially intuitive. Zeta potential of particles can be affected by multiple parameters, including particle size, morphology, and surface charge density. The charge density in the K5 ligand is higher than the charge density in the H3 ligand, whereas the H3 ligand contains more primary amines dispersed along a much longer peptide chain. In addition, the K5 ligands are buried beneath the longer H3 ligands when both are displayed on the gold surface, with the long chains of the H3 ligand presumably presenting mushroom-like morphologies. Therefore, the longer H3 chain likely contributes more significantly to the properties at the actual shear plane in solution. The evolution in hydrodynamic diameter as a function of peptide addition also is likely to contribute to the changing zeta potential in the different particle preparations. The lower zeta potential in the low H3-AuNPs as

Author Manuscript Author Manuscript Author Manuscript Author Manuscript

compared with the K5 AuNPs is likely due in part to the increased hydrodynamic diameter in the low-H3 AuNPs, which would lead to a relatively sparse zeta potential at the shear plane. As the number density of H3 ligands on the surface increased, the zeta potential of these nanoparticles increased accordingly.

Nanoscaffold Association with Histone Effector Complexes

Given our previous studies confirming the enhanced nuclear activities and histone effector binding capacities of H3-based polyplexes,[54] we asked whether improved H3 tail display on the surface of AuNPs enabled robust interactions with nuclear protein complexes. The H3 tail sequence interacts directly with transcription factors within the nucleus, including the HBO1 histone acetyltransferase (HAT) complex[55] that helps activate chromosomal DNA for transcription.[56] The HBO1-HAT complex binds to the H3 tail sequence and catalyzes acetylation of downstream lysine residues on the H3 tail,[55, 57, 58] thereby activating chromosomal DNA for transcription.[56, 59] Pull-down assays were employed to examine the interactions between the nanoscaffolds and HBO1. The nanoscaffolds were incubated with HBO1-enhanced cell lysates purified from human HEK293T cells, and the resulting binding to HBO1 was analyzed via Western blotting (Figure 5). As expected, AuNPs completely covered by the H3 tail ligand (high-H3 AuNPs; 67 ligands total) successfully pulled down HBO1. To confirm whether the interactions between AuNPs displaying the H3 tail and HBO1 were caused by sequence-specific interactions with H3 vs. non-specific electrostatic interactions, the ability of the K5 AuNPs to pull down HBO1 also was evaluated. As shown in Figure 5A, the K5 AuNPs displayed low levels of interaction with HBO1 when incubated with cell lysates. Densitometry analysis of band intensities (Figure 5B) revealed a ~3-fold higher association between HBO1 and the high-coverage histone-mimetic nanoscaffolds as compared to the unmodified K5 AuNPs.

The ability of the K5 AuNPs to pull down small amounts of HBO1 indicates that a small non-specific level of interaction exists between the modified AuNPs and HBO1, likely due to electrostatic interactions. It is reasonable to expect that some threshold of H3 tail display exists on the gold surface wherein specific H3 peptide interactions with HBO1 overcome non-specific electrostatic interactions. Moreover, AuNPs containing lower levels of H3 (low- and mid-H3 AuNPs) exhibited limited HBO1-HAT pull-down levels that were similar to the levels of K5 AuNP pull-down (not shown). We also noted that AuNPs pulled-down multiple protein bands detected by the HBO1 primary antibody (Figure 5A). This was attributed to different glycosylation tags occurring on the expressed HBO1 protein. The purchased HBO1-enhanced human cell lysate contained HBO1 with a FLAG tag attached to the C-terminus of the protein. Probing the same blot with anti-FLAG primary antibody reveals an identical band pattern (Figure S4), confirming that all bands represent the HBO1 protein, but with different levels of glycosylation.

Characterization and Stabilization of AuNP-pDNA Complexes

To assess the pDNA condensation and packaging effects of the nanoscaffolds, AuNP-pDNA complexes were prepared at a range of N:P ratios and the resulting complexes were evaluated by agarose gel electrophoresis and ethidium bromide staining. Complex formation was detected as a reduction in pDNA mobility in the gel as well as a reduction in staining,

Author Manuscript Author Manuscript Author Manuscript Author Manuscript

since the binding by the intercalating dye, ethidium bromide, is inhibited when pDNA is sufficiently condensed. The electrophoretic assay showed that all AuNPs formed stable complexes with pDNA above N:P = 1 (Figure 6), as indicated by the absence of pDNA mobility and ethidium bromide fluorescence. In contrast, polyplexes formed with the cationic polymer PEI (PEI-pDNA) displayed significantly lower binding and condensing capacity, requiring an N:P ratio of at least 4 before full pDNA condensation occurred. These results indicated that the modified AuNPs enabled enhanced pDNA binding as compared with typical polymeric transfection reagents. This was likely due to the improved presentation of primary amines on the gold surface, which form stronger electrostatic interactions with the negatively charged pDNA backbone than other amines due to their higher protonation at neutral pH.[60–62] Based on ligand composition (Table 1) the number of primary amines present on the surface of the modified AuNPs ranges from ~155 to ~603. In contrast, the number of primary amines on the branched PEI polymer is ~133.[63] The higher content and better access to primary amines on the AuNPs ultimately results in greater binding capacity and tighter complexes than those obtained with branched PEI, which contains a mixture primary and secondary amine groups.

To further assess pDNA complexation by the AuNPs, the hydrodynamic diameter of the complexes was measured to confirm that their size was within a reasonable range for efficient endocytosis.[64, 65] As shown in Table 2, increasing the N:P ratio led to reductions in the overall diameters of the AuNP-pDNA complexes as the pDNA became more efficiently condensed. A significant decrease in hydrodynamic diameter was observed as the N:P ratio increased from 1 to 2. These results are consistent with the agarose gel analyses. As the N:P ratio increased above 1, additional compaction of the complexes occurred, resulting in smaller and more uniform particles overall (Figure S5). The diameters of the AuNP-pDNA complexes were smaller than those of the PEI polyplexes at N:P ratios of 1 and 2 (PEI polyplexes do not form at an N:P = 1), which also corresponded well with the agarose gel electrophoresis results. Meanwhile, the zeta potentials of the H3 AuNP-pDNA complexes were all moderately positive (between 10–15 mV), which indicated that the negatively charged pDNA had incorporated enough AuNPs to reverse its surface charge; we suspect that for all H3 AuNP-pDNA complexes, the zeta potential was defined primarily by the extended H3 tails, which created a ‘screening’ effect. Further inclusion of a larger amount of AuNPs did not contribute much to an elevated zeta potential of the complexes, at least up to an N:P ratio of 4. However, the zeta potentials of the K5 AuNP complexes were substantially different from those of the H3 AuNP complexes, displaying a range from −34 to 50 mV when the N:P ratios increased from 1 to 4. The zeta potential difference between K5 AuNP and H3 AuNP based complexes is most likely due to the absence of the H3 tail ‘screening’ effect in the K5 AuNP complexes. The K5 AuNP complexes likely exhibited zeta potentials that were more reflective of the actual charge balance between the AuNP core ligands and the pDNA, resulting in a negative zeta potential at N:P=1 due to the lack of complete protonation of all lysine residues at neutral pH.[63]

Given the capacity of the AuNPs to more efficiently bind and condense pDNA at low N:P ratios, we investigated whether the AuNP-pDNA complexes were more resistant to heparin destabilization than polyplexes formed with PEI. AuNP-pDNA complexes were formed at an N:P ratio of 4 and incubated with increasing concentrations of heparin. Heparin is a

Author Manuscript Author Manuscript Author Manuscript Author Manuscript

common polyanionic glycosaminoglycan (GAG) found in extracellular matrix (ECM), and it (and other ECM polyanions) is known to displace nucleic acids from cationic delivery vehicles.[66] Thus, enhanced stability against heparin displacement is indicative of complexes that would be more stable under physiological conditions. As shown in Figure 7A–D, both K5 and H3 AuNP-pDNA complexes were resistant to heparin destabilization up to a heparin/pDNA wt/wt ratio of 1.0. Above this wt/wt ratio, the complexes began to loosen slightly and small quantities of pDNA were displaced, as indicated by the increase in ethidium bromide fluorescence in the wells and the increasing amount of pDNA migration down the gel. Slight variations in stability against heparin were observed between the different AuNP-pDNA complexes, with the high-H3AuNPpDNA complexes qualitatively appearing the most stable. These variations may be related to the changes in primary amine content and density between the modified AuNPs, with the high-H3 AuNPs possessing ~603 primary amines per particle and the K5, low-H3, and mid-H3 AuNPs possessing ~155, ~276, and ~265 amines per particle, respectively. In contrast, PEI polyplexes formed at the same overall charge ratio (Figure 7E) began to destabilize as early as a 0.25 heparin/pDNA wt/wt ratio. The pDNA was almost completely displaced from these PEI polyplexes at a 1.0 wt/wt ratio. These results further demonstrate the ability of both the K5 and histone-mimetic AuNPs to form stable complexes with pDNA that are resistant to destabilization from common ECM GAGs. The AuNP complexes required 4 times the amount of heparin as compared with the PEI polyplexes to initiate pDNA displacement. We hypothesize that the increase in primary amine content in combination with the modified peptide display on the AuNP surface enabled improved interactions with the anionic pDNA backbone, similar to native histone-chromatin interactions in the nucleus. These differences provided enhanced stability against native GAG displacement.

AuNP-pDNA Complex Transfection Efficiency

Given the enhanced capacity of both K5 AuNPs and histone-mimetic AuNPs to stably bind and condense pDNA, we next investigated their cellular transfection efficiency. Transfection studies were conducted in Chinese Hamster Ovary (CHO-K1) cells in either serum-free media or media supplemented with heparin at a concentration of 0.0025 mg/mL to simulate the physiological extracellular environment.[67] Based on our previous studies with H3-targeted nanocarriers,[64] we hypothesized that hybrid complexes formed with a known mediator of cellular uptake, such as PEI, in combination with the modified AuNPs would exhibit both robust stability in the extracellular environment as well as significant cellular accumulation. Transfection efficiencies of the hybrid complexes were analyzed by fluorescence microscopy (Figure 8A–B) and flow cytometry (Figure 8C–D). Complexes were formed at an overall ratio of N:P = 4, with an N:P = 1 contribution from the modified AuNPs and a N:P = 3 contribution from the PEI polymer. In the absence of heparin (Figure 8A), transfections with the K5 AuNP/PEI complexes produced insignificant levels of cells expressing the green fluorescent protein (GFP). In contrast, mixed complexes containing the high-H3 AuNPs transfected significantly more cells (Figure 8A and 8C). Additionally, the transfection efficiency of the high-H3 AuNP/PEI mixed complexes was similar to PEI-pDNA polyplexes formulated at the same overall charge ratio (N:P = 4). None of the tested mixed AuNP/PEI complexes nor PEI polyplexes had any significant effects on cellular viability (Figure S6).

Author Manuscript Author Manuscript Author Manuscript Author Manuscript

Studies have reported systemic concentrations of heparin in normal human sera to be ~0.0016 mg/mL.[67, 68] Localized concentrations of heparin and heparan sulfate in the extracellular space are likely higher, especially in areas of native tissue regeneration, as heparin plays an essential role in facilitating cell motility and growth factor sequestration.[69] Thus, the heparin concentrations used in these studies provide an effective benchmark for evaluating complex transfection efficiency under physiological conditions. Most notably, the presence of heparin in the transfection media did not have any significant effects on the overall transfection efficiency of the high-H3 AuNP/PEI hybrid complexes (Figure 8B and 8D). In contrast, heparin incubation completely eliminated the transfection potential of the PEI polyplexes, due to polyplex destabilization. These results demonstrate the utility of the histone-mimetic AuNPs in providing the necessary stability against pDNA displacement by native GAG concentrations in the extracellular environment.

The absence of GFP expression following K5 AuNP/PEI hybrid complex transfection, regardless of heparin concentration, provides evidence of the H3 tail functioning to improve interactions with intracellular trafficking, nuclear import, and transcriptional activation machinery to ultimately enhance gene expression. Transfections with low- and mid-H3 AuNP/PEI hybrid complexes yielded an insignificant number of GFP-expressing cells (Figure S7), regardless of heparin incubation. These results further indicate that there are likely a critical number of H3 tail ligands that must be displayed on the surface of the AuNPs before native histone effectors can be engaged, possibly because complexation with the pDNA inhibits access to a fraction of the H3 tails. Overall, the nanoscaffold transfection efficiency evaluations not only demonstrated the utility of the modified AuNPs to stabilize gene delivery complexes from extracellular disassembly and pDNA degradation, but also showed that tuning ligand surface display could effectively tune interactions with intracellular effectors to enhance overall gene delivery and expression.

Conclusions

In this study, we demonstrated that alkanethiol-coated AuNPs provide ideal scaffolds for the tunable display of histone H3 tail peptides, resulting in the creation of AuNP nanoscaffolds with a combination of superior pDNA binding affinity and a capacity to enhance gene transfer through engagement of histone effectors. Using Murray place exchange, a small library of modified AuNPs was created, each displaying different levels of the H3 tail peptide. TGA and elemental analysis were used to accurately demonstrate that the number density of peptide ligands on the nanoscaffolds could be easily varied over the full range from minimal peptide functionalization (e.g., low-H3 AuNPs with 4 ligands), to full functionalization (e.g., high-H3 AuNPs with 67 ligands). The modified AuNPs mimicked the natural dimensions and tail presentation of the native histone octamer.

Pull-down assays revealed that the improved display of the H3 tail peptide facilitated interactions with native histone effectors, and that these interactions could be tuned to achieve up to a 3-fold difference in binding by changing the amount of H3 tail displayed on the AuNP surface. Moreover, the modified AuNPs displayed enhanced pDNA binding and condensation at half the overall charge ratio when compared to common transfection reagents. The resulting AuNP-pDNA complexes were highly stable against heparin

Author Manuscript Author Manuscript Author Manuscript Author Manuscript

displacement, requiring nearly 4fold higher heparin concentrations before releasing pDNA as compared to PEI polyplexes. Complexes containing the high-H3 AuNPs also resulted in a 6-fold improvement in transfection efficiency when compared to complexes displaying lower levels of the H3 tail, suggesting their ability to engage native histone processing pathways. An unprecedented finding was that the transfection efficiency of these complexes remained unchanged in the presence of physiologically relevant amounts of heparin, whereas physiological heparin levels completely destabilized the PEI polyplexes and eliminated their ability to transfect cells. Such results demonstrate the utility in following an ordered and biologically-inspired design approach in order to enhance both the stabilization and efficacy of non-viral gene delivery vehicles. Our design approach addresses a key need for biospecific targeting that does rely on pathogenic capsids or proteins to impart activity, yet ultimately protects against extracellular degradation and better engages native intracellular trafficking and nuclear import machinery for improved gene transfer and expression.

Experimental Procedures

Materials

Hydrogen tetrachloroaurate tri-hydrate ($HAuCl_4 \cdot 3H_2O$), $NaBH_4$, C5-SH, and 11-bromoundecanoic acid were purchased from Sigma-Aldrich (St. Louis, MO). Triphenylmethyl mercaptan (Ph_3C-SH) and tetraoctylammonium bromide (TOAB) were purchased from Acros Organics (Waltham, MA). Fmoc-protected amino acids, O-Benzotriazole-N,N,N’,N’-tetramethyl-uronium-hexafluoro-phosphate (HBTU), hydroxybenzotriazole (HOBt), and N,N’-diisopropylcarbodiimide (DIC) were purchased from Novabiochem (Burlington, MA). H-Rink amide ChemMatrix® resin was purchased from PCAS Biomatrix (Quebec, Canada). Primary antibodies against the human HBO1 histone acetyltransferase complex (rabbit monoclonal IgG) and a C-terminal FLAG tag (mouse monoclonal IgG2a) were purchased from Abcam (Cambridge, MA) and Origene (Rockville, MD) respectively. Human HBO1-enhanced cell lysate purified from HEK293T cells was purchased from Origene. All other reagents were purchased from Fisher Scientific (Fairlawn, NJ). The gWIZ (5757 bp) mammalian expression vector coding for GFP was purchased from Genlantis (San Diego, CA). The plasmid was amplified in NEB 5α electrocompetent *Escherichia coli* purchased from New England Biolabs and purified with a QIAGEN EndoFree Maxi Kit (Valencia, CA), according to the manufacturer’s protocols.

Triphenylmethyl-Protected MUA Synthesis

Ph_3C-SH (11.06 g, 40 mmol) was dissolved in 50 mL of an ethanol/toluene (1:1) mixture, and NaOH (3.2 g, 80 mmol) in 50 mL of double deionized water (ddH_2O) was added. The above mixture was added to a stirred ethanol/toluene solution (1:1, 30 mL) of 11-bromoundecanoic acid (5.3 g, 20 mmol). The reaction mixture was stirred at room temperature for 16 h. A 1 M aqueous HCl solution was added dropwise into the mixture at 0 °C until a pH value between 2 and 3 was reached. The above mixture was washed with a saturated aqueous NaCl solution three times. The organic layer was separated, dried over anhydrous sodium sulfate and concentrated on a rotary evaporator. The product was purified using flash column chromatography over silica gel with a mixture of DCM:MeOH (98:2,

Author Manuscript Author Manuscript Author Manuscript Author Manuscript

v/v) as the mobile phase. The solvent was removed by vacuum to obtain the final product, triphenylmethyl-protected MUA (yield: 9.0 g, >75 %; nuclear magnetic resonance (NMR) shown in Figure S1).

Peptide Ligand Synthesis

The K5 and H3 tail peptides were synthesized using automated Fmoc solid phase peptide synthesis (SPPS) on a Tribute™ peptide synthesizer (Protein Technologies Inc., Tucson, AZ). The H3 tail peptide sequence incorporates residues 1–25 of the N-terminal tail of the H3 protein (ARTKQTARKSTGGKAPRKQLATKAA*KG*-$CONH_2$, where the italicized residues are exogenous residues added as a putative reactive handle). The exogenous glycine at the C-terminus acts as spacer between the resin and the exogenous 1-(4,4-dimethyl-2,6dioxacyclohexylidene)ethyl (Dde)-protected lysine residue used for MUA conjugation. Since standard SPPS proceeds in the opposing C- to N-terminal direction, the MUA must be attached at the beginning C-terminus before H3 peptide synthesis proceeds. Following F-moclysine(Dde)-OH attachment, the Dde protecting group was removed by the addition of a weak base, as described previously.[70] Briefly, 1.25 g of hydroxylamine hydrochloride (NH_2OH•HCl) (1.80 mmol) 0.918 g of imidazole (1.35 mmol) were dissolved in 5 mL of N-methyl-2-pyrrolidone (NMP) via sonication for 3 h. The resulting solution was diluted with 1 mL of DCM, added to the peptide-resin, and stirred for 3 h at room temperature. Following Dde-deprotection, the MUA ligand was conjugated to the primary amine on the lysine side chain using HOBt and DIC in dimethylformamide (DMF) while mixing (12 h, 23 °C). After MUA conjugation, synthesis of the H3 tail peptide was continued under standard SPPS conditions. This synthetic procedure ensured that the H3 tail sequence was presented in the correct N- to C-terminal direction when displayed on the AuNP surface.

Cleavage of the final H3-MUA peptide ligand from the resin was performed using a cocktail of 94:1:2.5:2.5 trifluoroacetic acid (TFA)/triisopropylsilane (TIS)/ddH_2O/1,2-ethanedithiol (EDT) for 2 h. Purification of the peptide was performed by reverse-phase high performance liquid chromatography (RP-HPLC) on a Prominence chromatography instrument (Shimadzu, Inc., Columbia, MD) equipped with a Viva C18 (4.2 mm × 50 mm, 5 mm particle diameter) column from Restek (Lancaster, PA). ddH_2O with 0.1% TFA (Solvent A) and acetonitrile with 0.1% TFA (Solvent B) were employed as HPLC solvents with a gradient of solvent B from 10%–35% over 50 min at a flow rate of 5 mL/min. The eluent absorbance was monitored at 210 nm. The $[M+H]^+$ was determined with matrix assisted laser desorption ionization-time of flight mass spectrometry (MALDI-TOF MS, Bruker Microflex), which showed primary peaks of m/z = 3010.9 (+1H) and m/z = 1505.9 (+2H) (Figure S2). Predicted molecular weight of the H3-MUA peptide ligand was 3009.1 Da.

The K5 (KKKKK-$CONH_2$) peptide sequence was also synthesized using SPPS. Following N-terminal Fmoc removal, triphenylmethyl-protected MUA was conjugated to the N-terminus of the K5 peptide using the same conditions described above. Cleavage of the K5-MUA peptide ligand from the resin was performed using a cocktail consisting of 88:5:5:2 TFA/phenol/ddH_2O/TIS (v/v) for 2 h. Purification of the peptide was performed similarly by RP-HPLC with a gradient of 0.1% TFA in ddH_2O (A) and 0.1% TFA in acetonitrile (B) as

Author Manuscript Author Manuscript Author Manuscript Author Manuscript

the mobile phase. The gradient was allowed to run from 10% B to 35% B over 50 min at a flow rate of 5 mL/min. Peptide elution was monitored by absorbance measurements at 210 nm. The $[M+H]^+$ was determined with electrospray ionization-mass spectrometry (ESI-MS) on a Thermo Finnigan LCQ MS (Waltham, MA), which showed major peaks of m/z = 858.7 (+1H), m/z = 880.7 (+1Na) and m/z = 430.1 (+2H) (Figure S3). Predicted molecular weight of the K5-MUA peptide ligand was 857.7 Da.

C5-AuNP Synthesis

The standard Brust-Schiffrin two-phase method[49] was used to synthesize C5 monolayer-protected AuNPs. Briefly, 30 mL of 30 mmol/L $HAuCl_4$ aqueous solution was added to 80 mL of 50 mmol/L TOAB toluene solution until all $AuCl_4^-$ was transferred to the organic phase and the aqueous phase turned fully clear. Subsequently, 1.8 mmol of C5-SH was added to the organic phase. Next, 25 mL of 18 mmol $NaBH_4$ aqueous solution was added rapidly into the reaction mixture. The mixture was stirred for 3 h at room temperature. The organic phase was collected and concentrated on a rotary evaporator. The concentrated AuNPs were purified by multiple acetone/ethanol washing and precipitation cycles as described previously.[71] The purified AuNPs were dried in a vacuum oven at room temperature. The final dry powder product was sealed under N_2 and stored at −20 °C.

K5/H3-Containing AuNP Preparation

The Murray place exchange reaction[50] was employed in two steps to replace the C5-SH monolayer with K5-MUA and H3-MUA peptide ligands. Briefly, C5 AuNPs (10 mg) were dissolved in 10 mL of DCM and the resulting mixture was purged with N_2; ~40 mg of K5-MUA peptide ligands were dissolved in 5 mL of DCM/MeOH mixture (4:1 v/v) and the resulting solution was also purged with N_2. Solutions of both the C5 AuNPs and K5-MUA ligands were mixed, and the resulting solution stirred for 3 days at room temperature. The solvents were roto-vapped under reduced pressure at 37 °C, and excess ligands were removed by washing 3X with DCM:MeOH (20:1 v/v) as well as dialysis against ddH_2O for 3 days (10 kDa molecular weight cut off). The aqueous suspension of K5 AuNPs was lyophilized to obtain a brownish solid product. H3 ligand-containing AuNPs were prepared by a second place exchange reaction using the K5 AuNPs and H3-MUA peptide ligands in ddH_2O for 3 days. 12, 23, or 45 mg of H3-MUA ligands were used to react with 10 mg of K5 AuNPs in a total of 20 mL ddH_2O to make the low-, mid-, and high-H3 AuNPs. Excessive ligands were removed by multiple washing and filtering cycles using AmiconUltra centrifugal filters (EMD Millipore, Burlington, MA) with a 10 kDa molecular weight cutoff.

AuNP Characterization

The core dimensions of the AuNPs were measured by bright-field TEM using a JEM3010 ultrahigh resolution analytical electron microscope at an accelerating voltage of 300 kV. The samples were prepared by pipetting ~5 μL of a 0.5 mg/mL AuNP solution onto carbon-coated copper grids and allowed to stand for 1 min. Excess solution was wicked away from the grid using clean filter paper. All samples were dried for at least 1 h before imaging.

Author Manuscript Author Manuscript Author Manuscript Author Manuscript

TGA was used to evaluate the total weight of organic ligands on the AuNP surfaces using a Discovery TGA (TA Instruments, New Castle, DE) at a heating rate of 10 °C/min under an N_2 atmosphere. The temperature ramping range was 25 °C−700 °C, and the ligand weight portion was calculated based on the weight loss using an assumption of spherical gold cores with a density of 19.3 g/cm^3.

CHNS elemental analysis was performed on AuNPs displaying 2 or more ligands on the surface. Analyses were performed by Intertek Pharmaceutical Services (Whitehouse, NJ) for the K5, low-H3, and mid-H3 AuNPs. Results were reported as the wt% of carbon, hydrogen, nitrogen, and sulfur relative to the entire sample analyzed (Table S1).

The Z-average hydrodynamic diameter and the zeta potentials of the AuNPs were analyzed using a Malvern or Wyatt Mobius DLS Zeta Potential Detector at 20 °C. Hydrodynamic diameter (based on cumulants analysis) and zeta potential analyses (employing the Smoluchowski model) were determined on sample data from 10 measurements of 2 min each for each sample.

HBO1 Pull-Down Assay

Free AuNP solutions at equivalent concentrations of positive charge were prepared in 150 μL of 20 mM HEPES buffer. 1.5 μL of a 100X Halt Protease solution was added to the AuNP solutions and the mixtures were incubated on ice for 10 min. Next, 6 μL of FLAG-tagged HBO1-enhanced cell lysate was added to each sample. Samples were gently mixed and agitated for 4 h at 4 °C. Protein corona-coated AuNPs were collected by ultracentrifugation for 1.5 h at 15,000 RPM.[72] Samples were washed with phosphate buffered saline (PBS) to remove the soft corona and the resulting pellets were resuspended in 30 μL PBS containing 5 μL Laemmli buffer and 3 μL β-mercaptoethanol. These solutions were boiled for 10 min and the denatured protein solutions were analyzed via sodium dodecyl sulfide-polyacrylamide gel electrophoresis on a 4%−40% acrylamide gel for 35 min at 150 V. Subsequently, the protein was transferred onto a poly(vinylidene fluoride) membrane for 75 min at 18 V. The membrane was blocked in 5 vol% non-fat milk in Tris-HCl buffered saline (50 mM Tris-HCl, pH 7.4, and 150 mM NaCl) containing 0.1 vol% Tween-20 (TBST) at room temperature for 1 h. The membrane was incubated with either anti-HBO1 (diluted 1/3000 in TBST) or anti-FLAG (diluted ½000 in TBST) at 4 ˚C overnight. The next day, the membrane was washed and incubated with a goat anti-rabbit or anti-mouse polyclonal IgG antibody conjugated to horseradish peroxidase (diluted 1/5000 in TBST) at room temperature for 1 h. Target proteins were visualized on a FluorChem® FC2 equipped with a Nikon Sigma EXDG camera (Cell Biosciences, Palo Alto, CA) after incubation with the SuperSignal West Dura Chemiluminescent Substrate.

AuNP-pDNA Complex Formation and Characterization

Complexes were formed by self-assembling pDNA with PEI or AuNPs. Briefly, equal volume solutions of pDNA and PEI/AuNPs were prepared in 20 mM HEPES at pH 6.0, and the PEI/AuNP solutions were added drop-wise to the pDNA solutions while vortexing so that the final pDNA concentration was 20 μg/mL. The PEI/AuNP concentrations in the mixtures were varied such that the N:P ratio, defined as the ratio of the number of amines

Author Manuscript Author Manuscript Author Manuscript Author Manuscript

(N) in the polymer to the number of phosphates (P) in the plasmid, would be as specified. The complex solutions were incubated for 10 min at room temperature to allow for self-assembly.

Hybrid AuNP/PEI complexes were prepared in a similar fashion. First, a solution of AuNPs at the indicated N:P ratio was added dropwise to a solution of pDNA while vortexing. The resulting solution was allowed to incubate at room temperature for 10 min. Subsequently, a solution containing the PEI polymer at the indicated N:P ratio was added to the intermediate AuNP-pDNA solution while vortexing. Again, complexation was allowed to proceed for 10 min at room temperature.

The hydrodynamic diameters and zeta potentials of the complexes at multiple N:P ratios were evaluated similarly to the free AuNPs, as described above. Samples were prepared in 20 mM HEPES, pH 6.0 at 20 μg/mL followed by a 2-fold dilution and filtration through 200 nm PVDF filters. Hydrodynamic diameters and zeta potentials were determined by intensity-weighted analysis on sample data from 10 measurements of 2 min each.

pDNA complexation was analyzed by agarose gel electrophoresis according to standard protocols. Briefly, a 1% agarose gel containing 0.5 μg of ethidium bromide/mL was formed in 1X tris/borate/ethylenediaminetetraacetic acid buffer. 20 μL of each complex solution was added to 5 μL of gel loading buffer and the resulting solutions were added to the gel well. Gels were run for 2 h at 100 V and imaged using a BioRad Gel Doc XR (Hercules, CA).

For heparin stability studies, complexes containing 0.5 μg of pDNA were formed as described above using either the modified AuNPs or PEI and the complexes were subsequently incubated with the indicated heparin solutions (over the reported ranged of heparin/pDNA wt/wt ratios) for 30 min at 37 °C. pDNA displacement was subsequently analyzed by gel electrophoresis as described above.

Transfection Efficiency and Flow Cytometry

CHO-K1 cells were obtained from the American Type Culture Collection (ATCC, Manassas, VA). The cells were cultured according to ATCC protocols at 37 °C and 5% CO_2 in Dulbecco's modified Eagle's medium (DMEM) supplemented with 10% fetal bovine serum and 1 % penicillin-streptomycin. For transfection, cells were seeded in multi-well plates at a density of 15,000 cells/cm^2. Immediately prior to transfection, the cells were washed in PBS and covered in Opti-MEM. Nano/polyplex solutions containing 1 μg of DNA/cm^2 well surface area were added dropwise to the cells 20 h post-seeding. After 2 h incubation with the transfection reagents, the cells were washed with PBS and cultured in 1 mL of fully supplemented media for an additional 24 h. When conducting transfection efficiency studies in the presence of heparin, a solution of heparin in ddH_2O was added to each well to a final concentration of 0.0025 mg/mL and incubated with the rest of the transfection reagents.

Cells were imaged on a Leica 6000 fluorescence microscope (Wetzler, Germany). GFP expression was quantified on a FACS Caliber Flow Cytometer (San Jose, CA). For cytometry analyses, cells were collected after imaging by standard trypsin mediated collection protocols. Cells were resuspended in PBS containing 0.2 vol% bovine serum

Author Manuscript Author Manuscript Author Manuscript Author Manuscript

albumin, filtered through 35 μm nylon mesh to remove aggregates, and stored at 4 °C until analysis. Scattering plots were gated for quantification purposes, and a total of 10,000 live cells were analyzed for each sample. Dead cells were excluded from transfection efficiency analyses.

Cell Viability and Live Cell Surface Coverage

Following the transfection protocols described above, both live and dead cells were visualized by fluorescence microscopy following staining with Calcein-AM and propidium iodide. Cells were washed twice with PBS at 24 h post-transfection and incubated in Opti-MEM containing 0.1 vol% Calcein-AM and propidium iodide for 50 min at 37 °C. The percent of viable cells was quantified by counting the number of live and dead cells using ImageJ analysis software.[73] Live cell surface coverage was also quantified using ImageJ analysis by counting the total number of live cells and scaling to the surface area of the well. All samples were analyzed relative to untransfected controls.

Statistical Analyses

Results for all plots are shown as the mean ± standard deviation of data obtained from at least three independently prepared and analyzed samples. Statistical analyses were performed using a Student's *t*-test or one-way analysis of variance. A value of $p < 0.05$ was considered to be statistically significant.

Supplementary Material

Refer to Web version on PubMed Central for supplementary material.

Acknowledgements

Funding: EVM and BF were supported by the National Institutes of Health under Grant No. 1R01EB017766. Any opinions, findings, and conclusions or recommendations expressed in this material are those of the authors and do not necessarily reflect the view of the National Institutes of Health.

Abbreviations

(AuNPs)	Gold nanoparticles
(K5-MUA)	5 lysine conjugated mercaptoundecanoic acid
(H3-MUA)	histone H3 tail conjugated mercaptoundecanoic acid
(pDNA)	plasmid DNA
(HBO1-HAT)	HBO1 histone acetyltransferase
(C5-SH)	1-pentanethiol
(PEI)	polyethylenimine
(TGA)	thermogravimetric analysis
(DLS)	dynamic light scattering

Author Manuscript Author Manuscript Author Manuscript Author Manuscript

(GAG)	glycosaminoglycan
(GFP)	green fluorescent protein

References

1. Khan I; Khan M; Umar MN; Oh DH, Nanobiotechnology and its applications in drug delivery system: a review. Iet Nanobiotechnology 2015, 9 (6), 396–400. [PubMed: 26647817]
2. Sharma N; Ojha H; Bharadwaj A; Pathak DP; Sharma RK, Preparation and catalytic applications of nanomaterials: a review. Rsc Advances 2015, 5 (66), 53381–53403.
3. Roco MC, The long view of nanotechnology development: the National Nanotechnology Initiative at 10 years. Journal of Nanoparticle Research 2011, 13 (2), 427–445.
4. Uddin I; Venkatachalam S; Mukhopadhyay A; Usmani MA, Nanomaterials in the Pharmaceuticals: Occurrence, Behaviour and Applications. Current Pharmaceutical Design 2016, 22 (11), 1472–1484. [PubMed: 26775674]
5. Blanco E; Shen H; Ferrari M, Principles of nanoparticle design for overcoming biological barriers to drug delivery. Nature Biotechnology 2015, 33 (9), 941–951.
6. Loh XJ; Lee TC; Dou QQ; Deen GR, Utilising inorganic nanocarriers for gene delivery. Biomaterials Science 2016, 4 (1), 70–86. [PubMed: 26484365]
7. Love JC; Estroff LA; Kriebel JK; Nuzzo RG; Whitesides GM, Self-assembled monolayers of thiolates on metals as a form of nanotechnology. Chemical Reviews 2005, 105 (4), 1103–1169. [PubMed: 15826011]
8. Hostetler MJ; Wingate JE; Zhong CJ; Harris JE; Vachet RW; Clark MR; Londono JD; Green SJ; Stokes JJ; Wignall GD; Glish GL; Porter MD; Evans ND; Murray RW, Alkanethiolate gold cluster molecules with core diameters from 1.5 to 5.2 nm: Core and monolayer properties as a function of core size. Langmuir 1998, 14 (1), 1730.
9. Giljohann DA; Seferos DS; Patel PC; Millstone JE; Rosi NL; Mirkin CA, Oligonucleotide loading determines cellular uptake of DNA-modified gold nanoparticles. Nano Letters 2007, 7 (12), 3818–3821. [PubMed: 17997588]
10. Verma A; Uzun O; Hu YH; Hu Y; Han HS; Watson N; Chen SL; Irvine DJ; Stellacci F, Surface-structure-regulated cell-membrane penetration by monolayer-protected nanoparticles. Nature Materials 2008, 7 (7), 588–595. [PubMed: 18500347]
11. Verma A; Stellacci F, Effect of Surface Properties on Nanoparticle-Cell Interactions. Small 2010, 6 (1), 12–21. [PubMed: 19844908]
12. Thakor AS; Jokerst J; Zavaleta C; Massoud TF; Gambhir SS, Gold Nanoparticles: A Revival in Precious Metal Administration to Patients. Nano Letters 2011, 11 (10), 4029–4036. [PubMed: 21846107]
13. Thakor AS; Paulmurugan R; Kempen P; Zavaleta C; Sinclair R; Massoud TF; Gambhir SS, Oxidative Stress Mediates the Effects of Raman-Active Gold Nanoparticles in Human Cells. Small 2011, 7 (1), 126–136. [PubMed: 21104804]
14. Connor EE; Mwamuka J; Gole A; Murphy CJ; Wyatt MD, Gold nanoparticles are taken up by human cells but do not cause acute cytotoxicity. Small 2005, 1 (3), 325–327. [PubMed: 17193451]
15. Pan Y; Neuss S; Leifert A; Fischler M; Wen F; Simon U; Schmid G; Brandau W; Jahnen-Dechent W, Size-dependent cytotoxicity of gold nanoparticles. Small 2007, 3 (11), 1941–1949. [PubMed: 17963284]
16. Thakor AS; Luong R; Paulmurugan R; Lin FI; Kempen P; Zavaleta C; Chu P; Massoud TF; Sinclair R; Gambhir SS, The Fate and Toxicity of Raman-Active Silica-Gold Nanoparticles in Mice. Science Translational Medicine 2011, 3 (79).
17. Hu J; Zheng PC; Jiang JH; Shen GL; Yu RQ; Liu GK, Sub-attomolar HIV-1 DNA detection using surface-enhanced Raman spectroscopy. Analyst 2010, 135 (5), 1084–1089. [PubMed: 20419260]
18. Mahmoud KA; Luong JHT, Impedance method for detecting HIV-1 protease and screening for its inhibitors using ferrocene-peptide conjugate/Au nanoparticle/single-walled carbon nanotube modified electrode. Analytical Chemistry 2008, 80 (18), 7056–7062. [PubMed: 18707132]

Author Manuscript Author Manuscript Author Manuscript Author Manuscript

19. Georganopoulou DG; Chang L; Nam JM; Thaxton CS; Mufson EJ; Klein WL; Mirkin CA, Nanoparticle-based detection in cerebral spinal fluid of a soluble pathogenic biomarker for Alzheimer's disease. Proceedings of the National Academy of Sciences of the United States of America 2005, 102 (7), 2273–2276. [PubMed: 15695586]
20. Eum NS; Yeom SH; Kwon DH; Kim HR; Kang SW, Enhancement of sensitivity using gold nanorods-Antibody conjugator for detection of E. coli O157:H7. Sensors and Actuators B-Chemical 2010, 143 (2), 784–788.
21. Duncan B; Kim C; Rotello VM, Gold nanoparticle platforms as drug and biomacromolecule delivery systems. Journal of Controlled Release 2010, 148 (1), 122–127. [PubMed: 20547192]
22. Pissuwan D; Niidome T; Cortie MB, The forthcoming applications of gold nanoparticles in drug and gene delivery systems. Journal of Controlled Release 2011, 149 (1), 65–71. [PubMed: 20004222]
23. Ghosh P; Han G; De M; Kim CK; Rotello VM, Gold nanoparticles in delivery applications. Advanced Drug Delivery Reviews 2008, 60 (11), 1307–1315. [PubMed: 18555555]
24. Wang HF; Huff TB; Zweifel DA; He W; Low PS; Wei A; Cheng JX, In vitro and in vivo two-photon luminescence imaging of single gold nanorods. Proceedings of the National Academy of Sciences of the United States of America 2005, 102 (44), 15752–15756. [PubMed: 16239346]
25. Durr NJ; Larson T; Smith DK; Korgel BA; Sokolov K; Ben-Yakar A, Two-photon luminescence imaging of cancer cells using molecularly targeted gold nanorods. Nano Letters 2007, 7 (4), 941–945. [PubMed: 17335272]
26. Maiorano G; Sabella S; Sorce B; Brunetti V; Malvindi MA; Cingolani R; Pompa PP, Effects of Cell Culture Media on the Dynamic Formation of Protein-Nanoparticle Complexes and Influence on the Cellular Response. Acs Nano 2010, 4 (12), 7481–7491. [PubMed: 21082814]
27. Ghosh PS; Kim CK; Han G; Forbes NS; Rotello VM, Efficient Gene Delivery Vectors by Tuning the Surface Charge Density of Amino Acid-Functionalized Gold Nanoparticles. Acs Nano 2008, 2 (11), 2213–2218. [PubMed: 19206385]
28. Thomas M; Klibanov AM, Conjugation to gold nanoparticles enhances polyethylenimine's transfer of plasmid DNA into mammalian cells. Proceedings of the National Academy of Sciences of the United States of America 2003, 100 (16), 9138–9143. [PubMed: 12886020]
29. Sullivan MMO; Green JJ; Przybycien TM, Development of a novel gene delivery scaffold utilizing colloidal gold-polyethylenimine conjugates for DNA condensation. Gene Therapy 2003, 10 (22), 1882–1890. [PubMed: 14502217]
30. Bonoiu AC; Mahajan SD; Ding H; Roy I; Yong KT; Kumar R; Hu R; Bergey EJ; Schwartz SA; Prasad PN, Nanotechnology approach for drug addiction therapy: Gene silencing using delivery of gold nanorod-siRNA nanoplex in dopaminergic neurons. Proceedings of the National Academy of Sciences of the United States of America 2009, 106 (14), 5546–5550. [PubMed: 19307583]
31. Ding Y; Jiang ZW; Saha K; Kim CS; Kim ST; Landis RF; Rotello VM, Gold Nanoparticles for Nucleic Acid Delivery. Molecular Therapy 2014, 22 (6), 1075–1083. [PubMed: 24599278]
32. Lee JS; Green JJ; Love KT; Sunshine J; Langer R; Anderson DG, Gold, Poly(beta-amino ester) Nanoparticles for Small Interfering RNA Delivery. Nano Letters 2009, 9 (6), 2402–2406. [PubMed: 19422265]
33. Mishra S; Webster P; Davis ME, PEGylation significantly affects cellular uptake and intracellular trafficking of non-viral gene delivery particles. European Journal of Cell Biology 2004, 83 (3), 97–111. [PubMed: 15202568]
34. Boisselier E; Astruc D, Gold nanoparticles in nanomedicine: preparations, imaging, diagnostics, therapies and toxicity. Chemical Society Reviews 2009, 38 (6), 1759–1782. [PubMed: 19587967]
35. Hahn MA; Singh AK; Sharma P; Brown SC; Moudgil BM, Nanoparticles as contrast agents for in-vivo bioimaging: current status and future perspectives. Analytical and Bioanalytical Chemistry 2011, 399 (1), 3–27. [PubMed: 20924568]
36. Chithrani BD; Ghazani AA; Chan WCW, Determining the size and shape dependence of gold nanoparticle uptake into mammalian cells. Nano Letters 2006, 6 (4), 662–668. [PubMed: 16608261]

Author Manuscript Author Manuscript Author Manuscript Author Manuscript

37. Dreaden EC; Alkilany AM; Huang XH; Murphy CJ; El-Sayed MA, The golden age: gold nanoparticles for biomedicine. Chemical Society Reviews 2012, 41 (7), 2740–2779. [PubMed: 22109657]
38. Peng LH; Huang YF; Zhang CZ; Niu J; Chen Y; Chu Y; Jiang ZH; Gao JQ; Mao ZW, Integration of antimicrobial peptides with gold nanoparticles as unique non-viral vectors for gene delivery to mesenchymal stem cells with antibacterial activity. Biomaterials 2016, 103, 137–149. [PubMed: 27376562]
39. Kim ST; Chompoosor A; Yeh YC; Agasti SS; Solfiell DJ; Rotello VM, Dendronized Gold Nanoparticles for siRNA Delivery. Small 2012, 8 (21), 3253–3256. [PubMed: 22887809]
40. Jiang Y; Tang R; Duncan B; Jiang Z; Yan B; Mout R; Rotello VM, Direct Cytosolic Delivery of siRNA Using Nanoparticle-Stabilized Nanocapsules. Angewandte Chemie-International Edition 2015, 54 (2), 506–510. [PubMed: 25393227]
41. Lee SK; Han MS; Asokan S; Tung CH, Effective Gene Silencing by Multilayered siRNA-Coated Gold Nanoparticles. Small 2011, 7 (3), 364–370. [PubMed: 21294265]
42. Ghosh P; Yang XC; Arvizo R; Zhu ZJ; Agasti SS; Mo ZH; Rotello VM, Intracellular Delivery of a Membrane-Impermeable Enzyme in Active Form Using Functionalized Gold Nanoparticles. Journal of the American Chemical Society 2010, 132 (8), 2642–2645. [PubMed: 20131834]
43. Mout R; Ray M; Tonga GY; Lee YW; Tay T; Sasaki K; Rotello VM, Direct Cytosolic Delivery of CRISPR/Cas9-Ribonucleoprotein for Efficient Gene Editing. Acs Nano 2017, 11 (3), 2452–2458. [PubMed: 28129503]
44. Bergen JM; Von Recum HA; Goodman TT; Massey AP; Pun SH, Gold nanoparticles as a versatile platform for optimizing physicochemical parameters for targeted drug delivery. Macromolecular Bioscience 2006, 6 (7), 506–516. [PubMed: 16921538]
45. Dixit V; Van den Bossche J; Sherman DM; Thompson DH; Andres RP, Synthesis and grafting of thioctic acid-PEG-folate conjugates onto Au nanoparticles for selective targeting of folate receptor-positive tumor cells. Bioconjugate Chemistry 2006, 17 (3), 603–609. [PubMed: 16704197]
46. Prabaharan M; Grailer JJ; Pilla S; Steeber DA; Gong SQ, Gold nanoparticles with a monolayer of doxorubicin-conjugated amphiphilic block copolymer for tumortargeted drug delivery. Biomaterials 2009, 30 (30), 6065–6075. [PubMed: 19674777]
47. Paciotti GF; Kingston DGI; Tamarkin L, Colloidal gold nanoparticles: A novel nanoparticle platform for developing multifunctional tumor-targeted drug delivery vectors. Drug Development Research 2006, 67 (1), 47–54.
48. Sun LL; Liu DJ; Wang ZX, Functional gold nanoparticle-peptide complexes as cell-targeting agents. Langmuir 2008, 24 (18), 10293–10297.
49. Brust M; Walker M; Bethell D; Schiffrin DJ; Whyman R, Synthesis of thiol-derivatized gold nanoparticles in a 2-phase liquid-liquid system. Journal of the Chemical Society-Chemical Communications 1994, (7), 801–802.
50. Hostetler MJ; Templeton AC; Murray RW, Dynamics of place-exchange reactions on monolayer-protected gold cluster molecules. Langmuir 1999, 15 (11), 3782–3789.
51. Green SJ; Pietron JJ; Stokes JJ; Hostetler MJ; Vu H; Wuelfing WP; Murray RW, Three dimensional monolayers: Voltammetry of alkanethiolate-stabilized gold cluster molecules. Langmuir 1998, 14 (19), 5612–5619.
52. Templeton AC; Wuelfing MP; Murray RW, Monolayer protected cluster molecules. Accounts of Chemical Research 2000, 33 (1), 27–36. [PubMed: 10639073]
53. Gibson JD; Khanal BP; Zubarev ER, Paclitaxel-functionalized gold nanoparticles. Journal of the American Chemical Society 2007, 129 (37), 11653–11661. [PubMed: 17718495]
54. Larsen JD; Reilly MJ; Sullivan MO, Using the Epigenetic Code To Promote the Unpackaging and Transcriptional Activation of DNA Polyplexes for Gene Delivery. Molecular Pharmaceutics 2012, 9 (5), 1041–1051. [PubMed: 22489650]
55. Saksouk N; Avvakumov N; Champagne KS; Hung T; Doyon Y; Cayrou C; Paquet E; Ullah M; Landry AJ; Cote V; Yang XJ; Gozani O; Kutateladze TG; Cote J, HBO1 HAT Complexes Target Chromatin throughout Gene Coding Regions via Multiple PHD Finger Interactions with Histone H3 Tail. Molecular Cell 2009, 33 (2), 257–265. [PubMed: 19187766]

Author Manuscript Author Manuscript Author Manuscript Author Manuscript

56. Strahl BD; Allis CD, The language of covalent histone modifications. Nature 2000, 403 (6765), 41–45. [PubMed: 10638745]

57. Strahl BD; Ohba R; Cook RG; Allis CD, Methylation of histone H3 at lysine 4 is highly conserved and correlates with transcriptionally active nuclei in Tetrahymena. Proceedings of the National Academy of Sciences of the United States of America 1999, 96 (26), 14967–14972. [PubMed: 10611321]

58. Hung T; Binda O; Champagne KS; Kuo AJ; Johnson K; Chang HY; Simon MD; Kutateladze TG; Gozani O, ING4 Mediates Crosstalk between Histone H3 K4 Trimethylation and H3 Acetylation to Attenuate Cellular Transformation. Molecular Cell 2009, 33 (2), 248–256. [PubMed: 19187765]

59. Palacios A; Moreno A; Oliveira BL; Rivera T; Prieto J; Garcia P; Fernandez-Fernandez MR; Bernado P; Palmero I; Blanco FJ, The Dimeric Structure and the Bivalent Recognition of H3K4me3 by the Tumor Suppressor ING4 Suggests a Mechanism for Enhanced Targeting of the HBO1 Complex to Chromatin. Journal of Molecular Biology 2010, 396 (4), 1117–1127. [PubMed: 20053357]

60. Ketola TM; Hanzlikova M; Leppanen L; Ravina M; Bishop CJ; Green JJ; Urtti A; Lemmetyinen H; Yliperttula M; Vuorimaa-Laukkanen E, Independent versus Cooperative Binding in Polyethylenimine-DNA and Poly(L-lysine)-DNA Polyplexes. Journal of Physical Chemistry B 2013, 117 (36), 10405–10413.

61. Ruponen M; Yla-Herttuala S; Urtti A, Interactions of polymeric and liposomal gene delivery systems with extracellular glycosaminoglycans: physicochemical and transfection studies. Biochimica Et Biophysica Acta-Biomembranes 1999, 1415 (2), 331–341.

62. Wong SY; Sood N; Putnam D, Combinatorial Evaluation of Cations, pH-sensitive and Hydrophobic Moieties for Polymeric Vector Design. Molecular Therapy 2009, 17 (3), 480–490. [PubMed: 19142180]

63. Tang MX; Szoka FC, The influence of polymer structure on the interactions of cationic polymers with DNA and morphology of the resulting complexes. Gene Therapy 1997, 4 (8), 823–832. [PubMed: 9338011]

64. Reilly MJ; Larsen JD; Sullivan MO, Histone H3 Tail Peptides and Poly(ethylenimine) Have Synergistic Effects for Gene Delivery. Molecular Pharmaceutics 2012, 9 (5), 1031–1040. [PubMed: 22280459]

65. Yue YA; Jin F; Deng R; Cai JG; Chen YC; Lin MCM; Kung HF; Wu C, Revisit complexation between DNA and polyethylenimine - Effect of uncomplexed chains free in the solution mixture on gene transfection. Journal of Controlled Release 2011, 155 (1), 67–76. [PubMed: 21056067]

66. Ruponen M; Ronkko S; Honkakoski P; Pelkonen J; Tammi M; Urtti A, Extracellular glycosaminoglycans modify cellular trafficking of lipoplexes and polyplexes. Journal of Biological Chemistry 2001, 276 (36), 33875–33880. [PubMed: 11390375]

67. Engelberg H, Plasma heparin levels in normal man. Circulation 1961, 23 (4), 578–&. [PubMed: 13696820]

68. Warren C; Manley G, Measurement of heparan-sulfate in normal human-serum by laser nephelometry. Clinica Chimica Acta 1984, 137 (3), 355–359.

69. Sarrazin S; Lamanna WC; Esko JD, Heparan Sulfate Proteoglycans. Cold Spring Harbor Perspectives in Biology 2011, 3 (7).

70. Diaz-Mochon JJ; Bialy L; Bradley M, Full orthogonality between Dde and Fmoc: The direct synthesis of PNA-peptide conjugates. Organic Letters 2004, 6 (7), 1127–1129. [PubMed: 15040739]

71. Moyano DF; Duncan B; Rotello VM, Preparation of 2 nm Gold Nanoparticles for In Vitro and In Vivo Applications In Nanomaterial Interfaces in Biology: Methods and Protocols, Bergese P; HamadSchifferli K, Eds. Humana Press Inc: Totowa, 2013; Vol. 1025, pp 3–8.

72. Monopoli MP; Pitek AS; Lynch I; Dawson KA, Formation and Characterization of the Nanoparticle-Protein Corona In Nanomaterial Interfaces in Biology: Methods and Protocols, Bergese P; HamadSchifferli K, Eds. Humana Press Inc: Totowa, 2013; Vol. 1025, pp 137–155.

73. Schneider CA; Rasband WS; Eliceiri KW, NIH Image to ImageJ: 25 years of image analysis. Nature Methods 2012, 9 (7), 671–675. [PubMed: 22930834]

Author Manuscript Author Manuscript Author Manuscript Author Manuscript

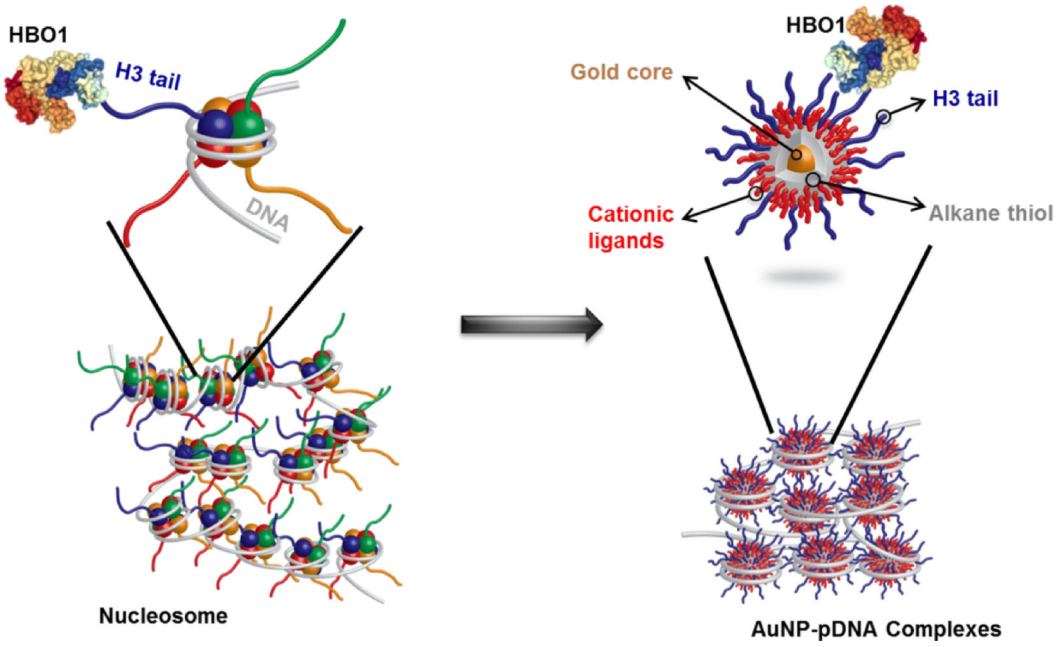

Figure 1:

Schematic illustration of the biomimetic design of H3-modified AuNPs that mimic the structure of native histone octamers. The HBO1-HAT transcriptional activator protein interacts with the H3 tail on both the native histone octamer (left) and the AuNPs (right).

Author Manuscript Author Manuscript Author Manuscript Author Manuscript

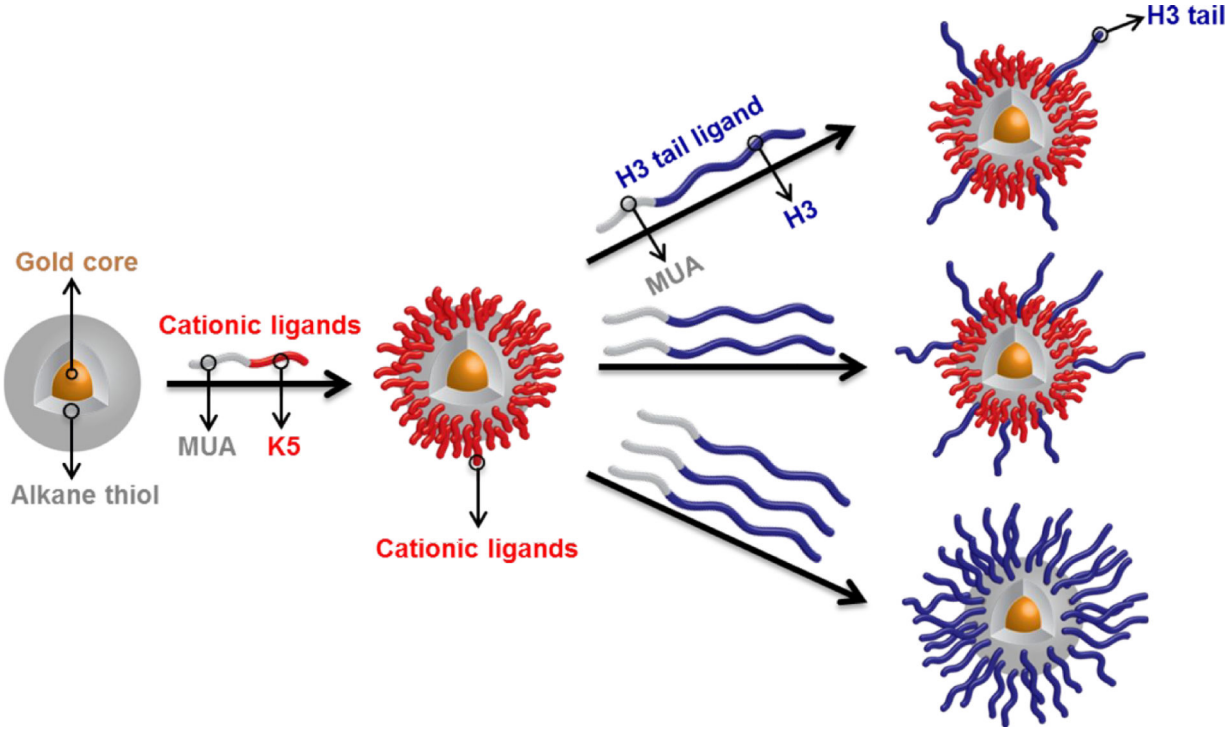

Figure 2:

Schematic illustration of the 2-step Murray place exchange strategy for ligand installation. Different number densities of H3 tail ligands are controlled by the H3 tail ligand feed ratio. MUA = mercaptoundecanoic acid; K5 = 5-residue polylysine peptide; H3 = H3 tail peptide (residues 1–25)

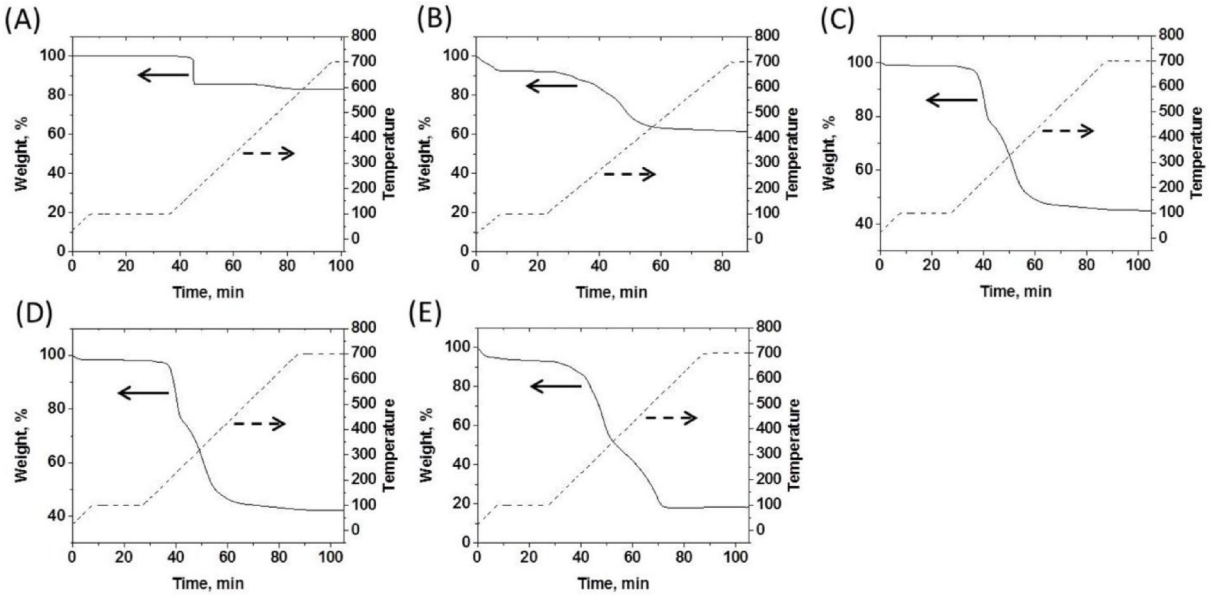

Figure 3:

TGA analysis of (A) C5 AuNPs; (B) K5 AuNPs; (C) Low-H3 AuNPs; (D) Mid-H3 AuNPs; (E) High-H3 AuNPs. Solid lines = weight percent data; dashed lines = temperature traces.

Author Manuscript Author Manuscript Author Manuscript Author Manuscript

Author Manuscript Author Manuscript Author Manuscript Author Manuscript

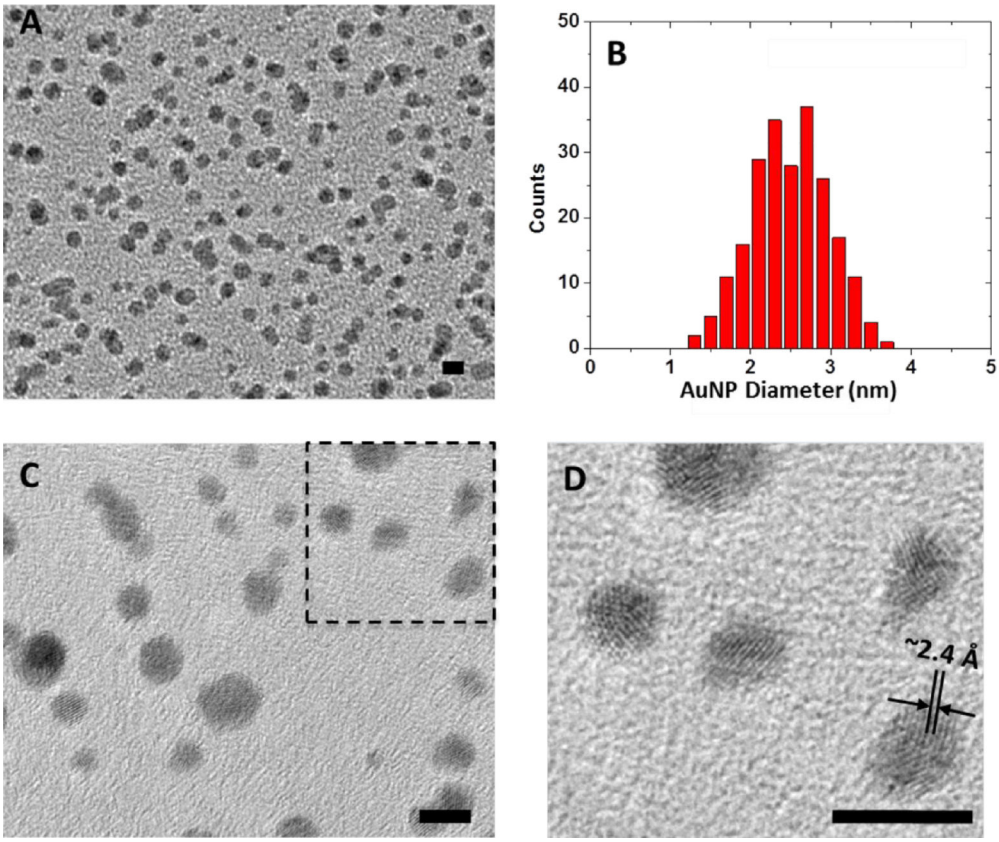

Figure 4:

TEM images of C5 AuNPs and the statistical analysis of AuNP core diameter. (A) Wide view image of the AuNPs; (B) Core diameter statistical analysis of all the AuNPs in (A), average core diameter = 2.5 nm; (C) magnified image of the AuNPs; (D) high-magnification image of the rectangular region in (C) showing the fine lattice structures of the gold cores. Scale bar in all images = 5 nm.

Author Manuscript Author Manuscript Author Manuscript Author Manuscript

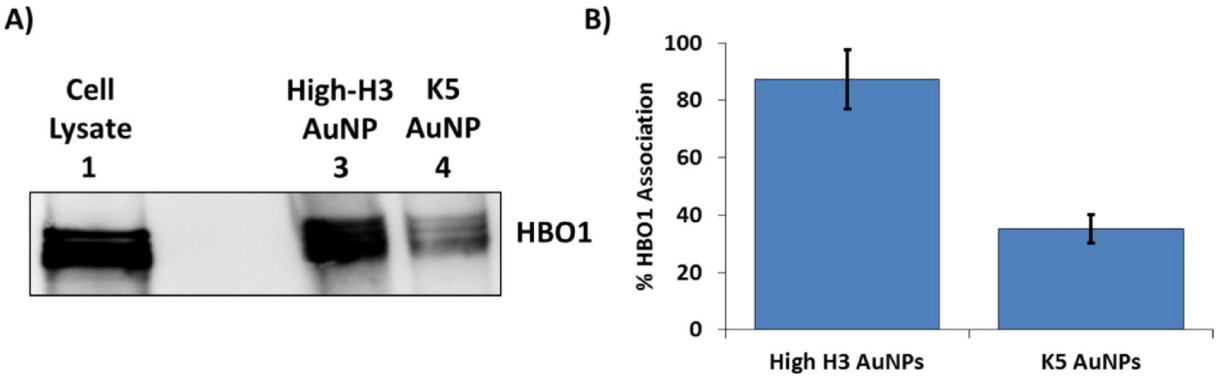

Figure 5:

HBO1 pull-down assay. (A) Representative Western blot image against HBO1 following HBO1 pull-down from HBO1-enhanced cell lysates using high-H3 and K5 AuNPs. Lane 1 is a sample of lysate proteins that were not incubated with AuNPs. Lanes 3 and 4 contain samples of lysate proteins that associated with the indicated AuNPs during the pull-down. (B) Densitometry analysis of Western blot band intensities using ImageJ, representing the amount of HBO1 association relative to the amount of HBO1 in the cell lysate control (lane 1). Results are shown as the mean ± standard deviation of data collected from three independent experiments.

Author Manuscript Author Manuscript Author Manuscript Author Manuscript

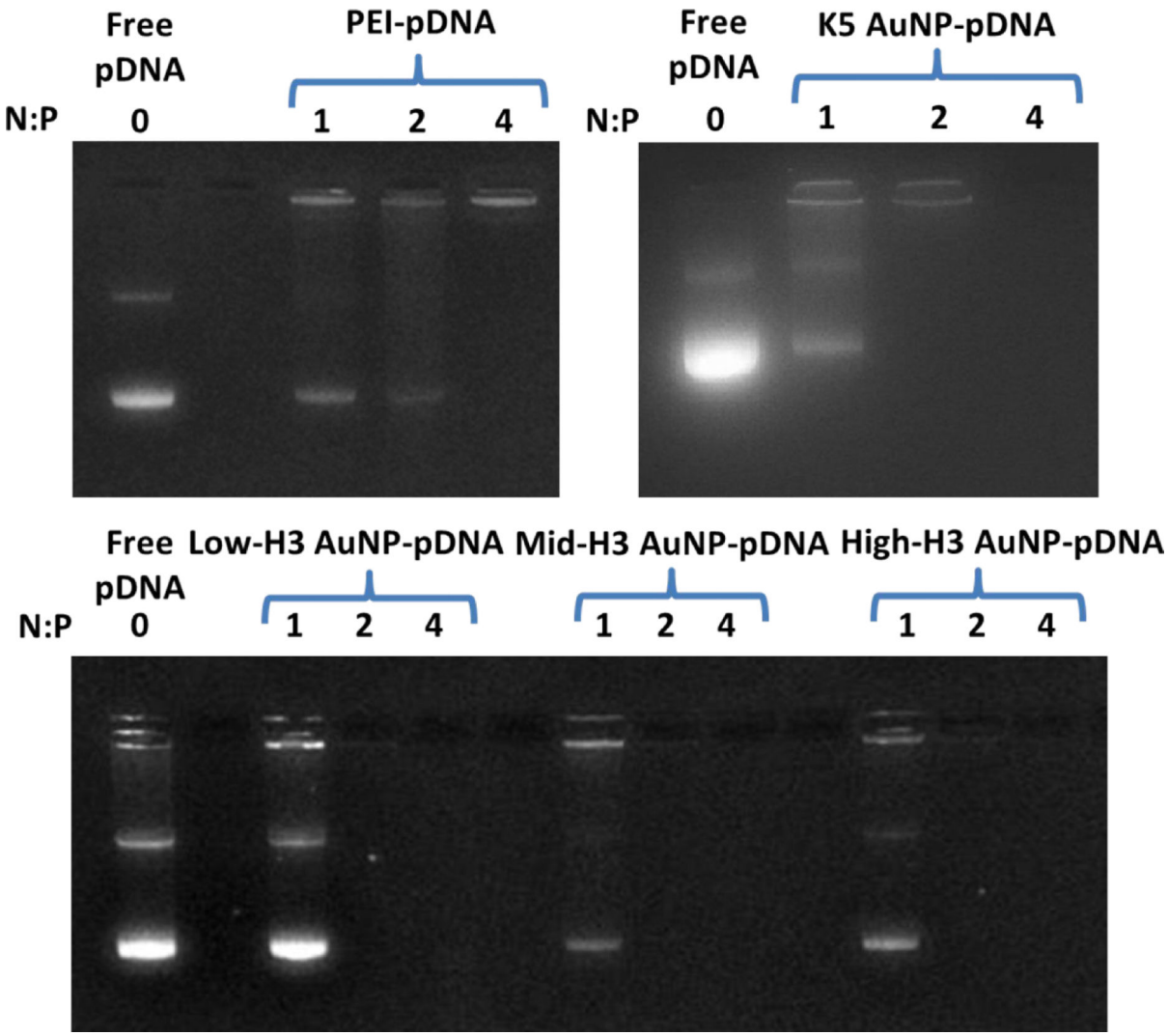

Figure 6:

pDNA binding analyses using agarose gel electrophoresis with ethidium bromide staining. The AuNP-pDNA complexes and PEI-pDNA polyplexes were formulated at the indicated N:P ratios.

Author Manuscript Author Manuscript Author Manuscript Author Manuscript

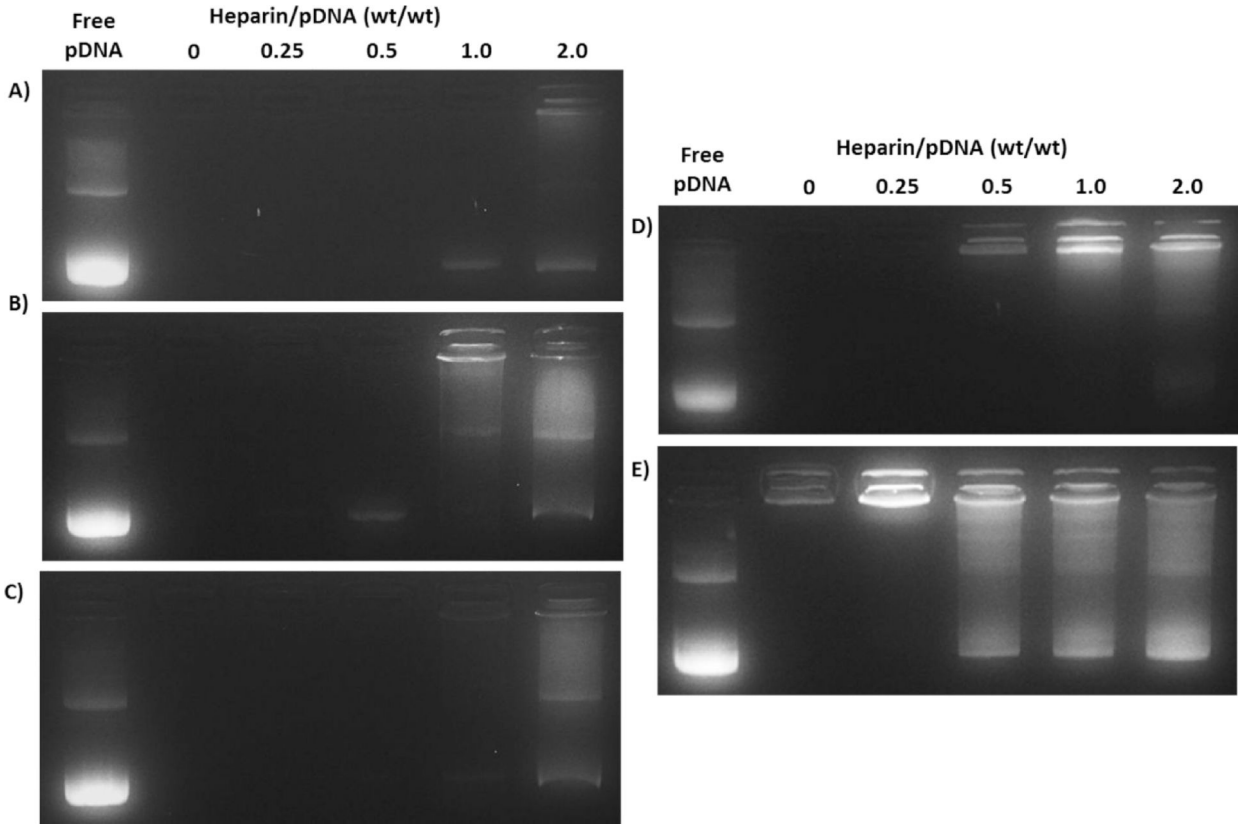

Figure 7:

Heparin displacement analysis of A) high-H3 AuNP complexes; B) mid-H3 AuNP complexes; C) low-H3 AuNP complexes; D) K5 AuNP complexes; and E) PEI polyplexes, all at an N:P ratio of 4. The AuNP-pDNA complexes and PEI polyplexes were incubated in the presence of increasing amounts of heparin for 0.5 h at 37 °C and the incubated samples were subsequently analyzed by agarose gel electrophoresis.

Author Manuscript Author Manuscript Author Manuscript Author Manuscript

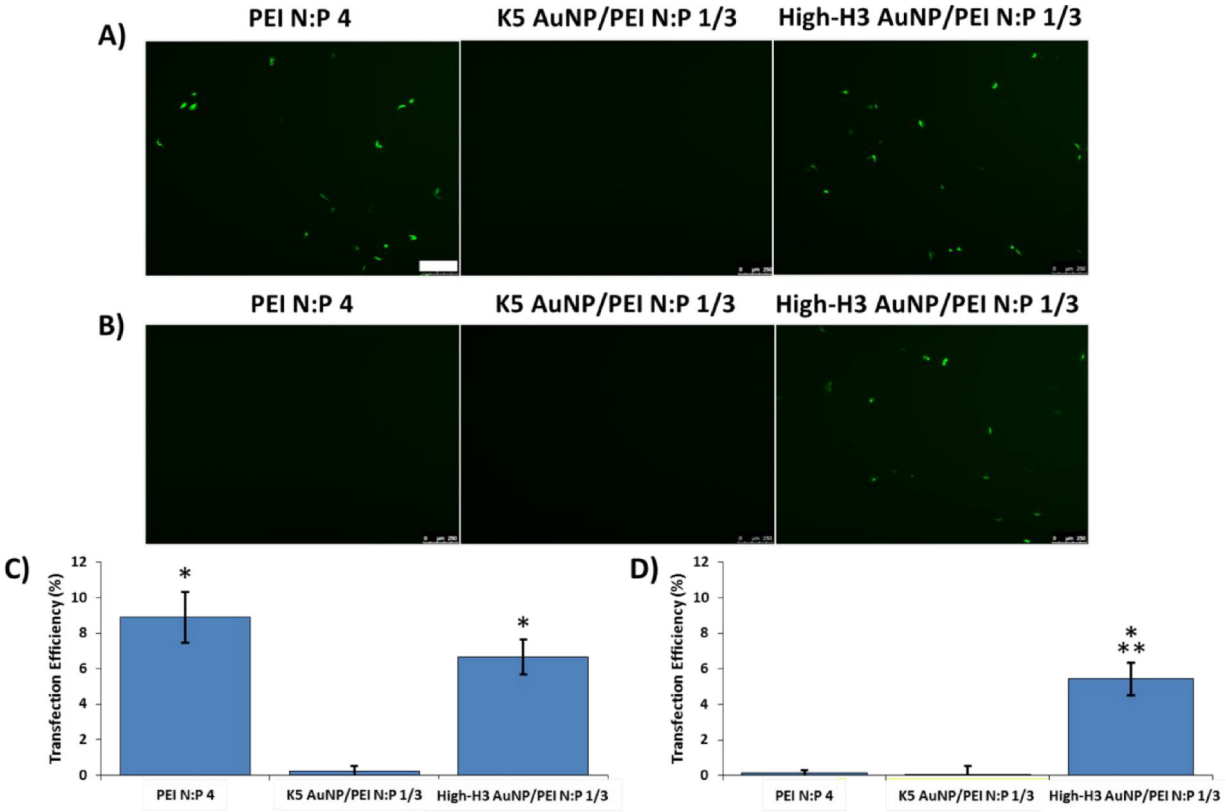

Figure 8:

CHO-K1 transfection with GFP-encoding pDNA. Representative fluorescence microscopy images of GFP expression 24 h post-transfection with the indicated hybrid AuNP complexes or PEI polyplexes either (A) without or (B) with heparin. Complexes were formed at an overall N:P ratio of 4, with an N:P = 1 contribution from the AuNPs and a N:P = 3 contribution from the PEI. Quantification of transfection efficiency (C) without or (D) with heparin using flow cytometry. All results are shown as the mean ± standard deviation of data collected from three independent experiments. * indicates a significant difference from zero ($p < 0.05$). ** indicates a significant difference from PEI polyplexes. Scale bar = 250 μm.

Author Manuscript

Author Manuscript

Author Manuscript

Author Manuscript

Table 1:

Surface property characterization of the synthesized AuNPs. Ligand compositions were measured using a combination of TGA and CHNS analysis. Hydrodynamic diameter and zeta potential measurements were assessed in HEPES buffer (pH 6.0).

Sample	Ligand Composition	Ligand #/AuNP	Hydrodynamic Diameter (nm)	Zeta Potential (mV)
C5 AuNP	C5	96	--	--
K5 AuNP	K5	31	22±1	36±3
Low-H3 AuNP	K5 & H3	48 (K5), 4(H3)	59±4	25±2
Mid-H3 AuNP	K5 & H3	35 (K5), 10 (H3)	74±3	43±2
High-H3 AuNP	H3	67	99±3	51±2

Author Manuscript Author Manuscript Author Manuscript Author Manuscript

Table 2:

Hydrodynamic diameters and zeta potentials of AuNP-pDNA complexes and PEI polyplexes at different N:P ratios using DLS analysis. All measurements were conducted in HEPES buffer.

Complex Sample	N:P	Hydrodynamic Diameter (nm)	Zeta Potential (mV)
Low-H3 AuNP-pDNA	1	353±214	11±2
	2	104±1	15±3
	4	81±0.4	13±4
Mid-H3 AuNP-pDNA	1	185±90	12±3
	2	101±1	14±5
	4	89±1	15±3
High-H3 AuNP-pDNA	1	105±1	11±2
	2	77±1	8±4
	4	80±1	11±3
K5 AuNP-pDNA	1	219±3	−34±2
	2	152±1	49±3
	4	134±3	50±3
PEI-pDNA polyplexes	1	--	--
	2	216±6	−10±5 *
	4	116±3	10±2 *

* From Reilly MJ, et. al., *Mol Pharm.* 9(5), 1031–40. 2012.[64]